SCALING EFFECTS ON FLOW FIELD AND ICE ACCRETION FOR A ROTATING WIND TURBINE BLADE

Galal M. Ibrahim[1], Greg F. Naterer[2], Kevin Pope[3]
Department of Mechanical Engineering, Memorial University of Newfoundland, St. John's, NL, Canada
[1,*] gmi588@mun.ca, [2] gnaterer@mun.ca, [3] kpope@mun.ca

Abstract A numerical study is presented in this paper to investigate blade sections (NACA 4415) with a scaling analysis. For variable rotational speeds (up to 60 RPMs) and operating/icing conditions for both similar models, the effects on the flow field, droplet impingement and ice accretion process are obtained. The numerical simulations are conducted using ANSYS FENSAP ICE software. Effects of the relative flow Reynolds number and speed ratio over two similar blade sections are investigated. Flow velocity contours, pressure distributions, droplet impingement/collection efficiencies and ice shapes/quantities are presented. The results of this paper provide useful insight to predict icing on wind turbine blades including scaling effects among different blade configurations.

Keywords *Scaling, rotating, atmospheric icing, numerical predictions*

I. INTRODUCTION

Ice accretion on wind turbine blade rotors in cold and moist conditions is a critical challenge which can significantly affect the performance of wind turbine operation [1]. Ice formation on a rotating wind blade can occur when supercooled water droplets in the atmosphere impinge on the blade surface [2]. Due to the large size of wind turbine blade rotors, it is difficult to investigate icing on full-size wind turbines in a laboratory facility. Thus, scaling methods can be an effective way to examine the icing characteristics on a wind blade surface. Similar scaling methods are used in the aerospace industry for aerodynamic scaling of aircraft [3].

CFD numerical simulations can be used to predict the impacts of icing on wind turbines operating in cold environments [4-6]. Atmospheric conditions in which high liquid water content and low temperatures near the freezing point, or environments with high convective cooling rates, can significantly impact wind turbine performance [7]. The formed ice mechanisms are influenced by the atmospheric conditions and usually divided into two main types [8]. Rime ice develops when impinging water freezes upon impact with the object surface, usually when the temperature is significantly below the freezing temperature. Glaze ice occurs in warmer conditions in which impinged droplets partially freeze on contact with the object surface while the remaining water gradually freezes when running back further downstream along the object surface [8].

The icing freezing process is strongly influenced by the cooling effect of the surrounding air, and by the energy released through evaporation. When the local temperature is near the freezing point, only a fraction of the water droplets freezes upon impact with an exposed surface. The remaining water is free to run back and freeze downstream, driven by shear stresses, gravity and in the case of wind turbines, rotational forces [9]. Ice accretion can degrade the aerodynamic characteristics of a rotating wind turbine rotor [10, 11]. Previous research indicated that the wind turbine rotor angular speed has a significant impact on the ice quantity [12, 13]. Combined changes in blade section chord length and relative flow velocity can significantly affect the ice accretion process. In this paper, variable rotational speeds and operating/icing conditions are investigated on two similar blade section models.

II. METHODOLOGY

A. *Formulation of flow, droplet and icing process equations*

Numerical modeling of an icing event around an object is achieved in ANSYS FENSAP ICE by solving firstly the air flow field around the blade using the FENSAP solver. This solves the partial differential equations for the conservation of mass, momentum and energy. The continuity equation for the carrier air phase is given by:

$$\frac{D\rho_a}{Dt} + \vec{\nabla} \cdot \left(\rho_a \vec{V_a}\right) = 0$$

(1)

The continuity equation for the dispersed droplet phase is:

$$\frac{D\alpha}{Dt} + \vec{\nabla} \cdot \left(\alpha \vec{V_d}\right) = 0$$

(2)

where α and V_d are the water volume fraction and droplet velocity, respectively. The Navier-Stokes equation is:

$$\frac{\partial \rho_a \vec{V_a}}{\partial t} + \vec{\nabla} \cdot \left(\rho_a \vec{V_a}\vec{V_a}\right) = \rho_a \vec{g} - \nabla p_a + \mu_a \nabla^2 \vec{V_a}$$

(3)

where ρ_a is the air density, V_a is the air velocity. The air conservation of energy equation can be written as:

$$\frac{\partial \rho_a E_a}{\partial t} + \vec{\nabla} \cdot \left(\rho_a \vec{V_a} H_a\right) = \rho_a \vec{g}.\vec{V_a} + \vec{\nabla} \cdot \left(k_a\left(\vec{\nabla} T_a\right) + v_i \tau^{ij}\right)$$

(4)

where E_a, H_a, and k_a are the internal energy, enthalpy and the thermal conductivity, respectively. Then by solving the droplet momentum equation, the droplet collection efficiencies are obtained by using a DROP 3D solver. The Navier-Stokes equation in the droplet phase becomes:

$$\frac{\partial\left(\alpha\vec{V_d}\right)}{\partial t} + \vec{\nabla} \cdot \left(\alpha\vec{V_d}\vec{V_d}\right) = \left(\frac{C_D \cdot Re_d}{24 K_d}\right)\alpha V_{a,\infty} + \alpha\left(1 - \frac{\rho_a}{\rho_d}\right)\frac{1}{Fr^2}$$

(5)

where K_d is droplet inertia parameter, and Re_d is the droplet-based Reynolds number; which are defined as:

$$K_d = \frac{\rho_d d_d{}^2 V_{a,\infty}}{18\mu_a c}$$

(6)

$$Re_d = \frac{\rho_a d_d V_{a,\infty}}{\mu_a}$$

(7)

The collection efficiency can be defined as:

$$\beta = -\frac{\alpha\vec{V_d}.\vec{n}}{LWC\ V_{a,\infty}}$$

(8)

where α is the local water volume fraction and n is the surface normal vector. The thermodynamics of the icing/freezing process uses ICE 3D to compute the ice mass quantities and predict ice shapes, and determine the freezing fraction and the energy transfer rates due to total water impinged, convection heat transfer, evaporation/sublimation, radiation, sensible heat and energy of ice formation.
The Reynolds number for the air flow can be calculated by:

$$Re_a = \frac{\rho_a V_{a,\infty} c}{\mu_a}$$

(9)

where $V_{a,\infty}$ is the relative flow stream velocity (includes both rotational and linear speeds). The total mass of water impingement can be calculated by:

$$M_{imp} = V_{a,\infty} LWC A_{imp} \beta t$$

(10)

The freezing fraction f, can be defined as the proportion of the total mass of liquid entering the control volume that freezes in that control volume, expressed as:

$$f = \frac{M_{ice}}{M_{imp}}$$

(11)

B. Computational domain and mesh discretization

CFD numerical analysis of the air flow, droplet impingement and ice accretion in this article are obtained with an ANSYS FENSAP-ICE solver. For each model, a hybrid computational mesh is constructed. Boundary conditions for the cylindrical domain (see Fig. 1) include the inlet, exit, slip outer wall and inner non-slip walls for the blade section. Fine grid elements with a first boundary layer thickness of 1×10^{-5} m over the blade section surface with a growth rate of 1.1 are constructed. Each NACA 4415 blade section is located at a one-third position from the inlet boundary to avoid reversed flow in the wake region and successfully achieve a converged solution. Steady-state simulations are achieved using a rotating frame of reference method. A one-equation Spalart Allmaras turbulence model is used for modeling the turbulent flow around the blade section. Convergence for air flow and droplet residuals are achievied.
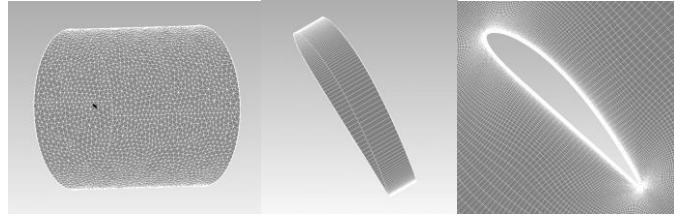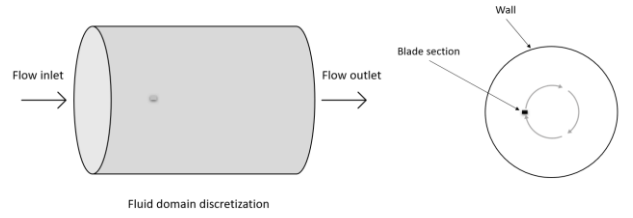

Figure 1. Discretization of cylindrical domain with the flow inlet, flow outlet and slip wall condition.

C. Test conditions

Two similar blade geometries are considered in this study – Model A: (Chord 0.5 m, Spanwise 0.1 m) and Model B: (Chord 1 m, Spanwise 0.2 m). The two similar models, NACA 4415 blade sections, have a scale factor of 2. Each blade model is located at a distance from the axis of rotation and rotates in the clockwise direction. The same icing condition is applied on both models. Each section is tilted at an angle of 45 degrees. The simulated test case conditions (case 1) for a variable rotational speed investigation are shown in Table 1.

TABLE 1. CASE 1 TEST CONDITIONS

Parameter	Value
Wind speed [m/s]	10
Rotational speed [RPM]	0, 10, 20, 30, 40, 50, 60
Rotational distance [m]	1
Icing temperature [°C]	-6
Liquid water content [g/m³]	5
Icing time [mins]	30
Droplet size [µm]	50

The simulated test conditions for case 2, which maintain a relative Reynolds number and speed ratio over each blade model, are shown in Table 2.

TABLE 2. CASE 2 TEST CONDITIONS

Parameter	Model A	Model B
Wind speed [m/s]	18.1	9.1
Rotational speed [RPM]	35	18
Relative speed [m/s]	25.6	12.8
Rotational distance [m]	5	
Icing temperature [°C]	-6	
Liquid water content [g/m^3]	1	
Icing time [mins]	60	
Droplet size [µm]	30	
Reynolds number	10^6	
Speed ratio	1	

III. RESULTS AND DISCUSSION

This section discusses and analyses the significant changes in the mixed flow field (air and droplets) during an icing event on two NACA 4415 similar blade sections which share a scale factor. Significant changes are compared at different operating/icing conditions.

A. Air and droplet flow fields

For case 1, air and droplet velocity contours are obtained for the two similar blade sections using FENSAP ICE and DROP 3D solvers, at different rotational speeds, as shown in Fig. 2. Droplet contours are like air velocity contours but with slightly different ranges. Only air velocity contours with legends are shown and both air and droplet velocity ranges are written under each contour. Results show minimal changes in the velocity upper magnitude. The results indicate that with a faster blade rotation, there is more flow attachment to the blade suction side, and thus more lift can be developed. At the same operating conditions in terms of rotational speed, distance from the rotation and linear wind speed, the velocity contours over similar blade sections remain almost the same.
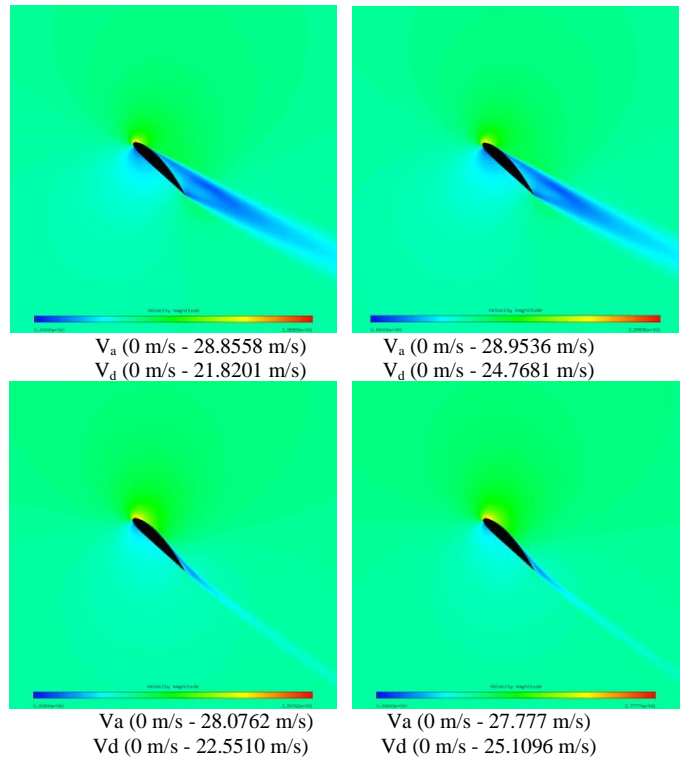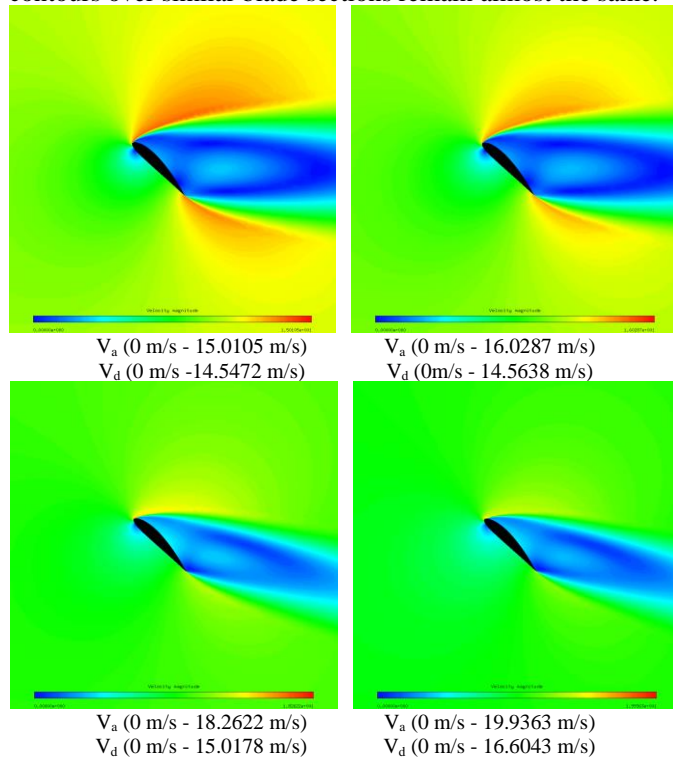

V_a (0 m/s - 15.0105 m/s)
V_d (0 m/s -14.5472 m/s)

V_a (0 m/s - 16.0287 m/s)
V_d (0m/s - 14.5638 m/s)

V_a (0 m/s - 18.2622 m/s)
V_d (0 m/s - 15.0178 m/s)

V_a (0 m/s - 19.9363 m/s)
V_d (0 m/s - 16.6043 m/s)

V_a (0 m/s - 28.8558 m/s)
V_d (0 m/s - 21.8201 m/s)

V_a (0 m/s - 28.9536 m/s)
V_d (0 m/s - 24.7681 m/s)

Va (0 m/s - 28.0762 m/s)
Vd (0 m/s - 22.5510 m/s)

Va (0 m/s - 27.777 m/s)
Vd (0 m/s - 25.1096 m/s)

Figure 2. Flow field around Model A (left) and Model B (right) at variable RPM (air and droplet velocity ranges).

B. Pressure distribution

For case 1, pressure coefficients over two similar blade sections are obtained at different rotational speeds. As shown in Fig. 3, plots are presented for a comparison between the models. For both model sections, slight changes are present in the pressure coefficient along the pressure and suction sides of the blade section surfaces. The blade's top surface represents the suction side (i.e. negative values) and the blade's bottom surface represents the pressure side (i.e. positive values). Results show that at lower rotational speeds, lower values for the pressure are expected on the suction side of a blade section.
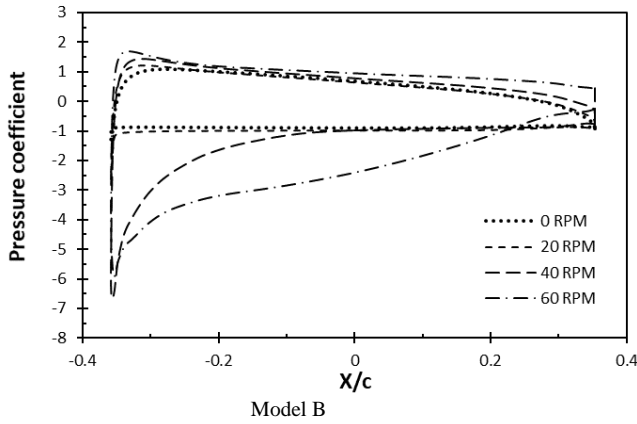

Model A
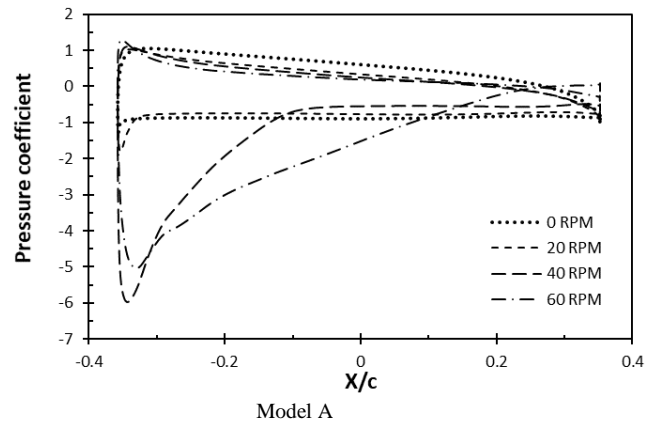
Figure 3. Pressure coefficient plots at variable RPMs.

C. Droplet impingiment/collection

The total collection efficiency is a measure of the total water collected by the object (i.e. airfoil). This is a ratio of the actual mass of impinging water to the maximum value that would occur if the droplets followed straight-line trajectories. For case 1, collection efficiency plots are obtained for both similar blade sections (Fig. 4). Results indicate that for Blade Model A (i.e. smaller blade section), higher collection efficiency values are predicted when compared to Model B (i.e. larger blade section). Also, results show that at lower rotational speeds, lower collection efficiency values are predicted.
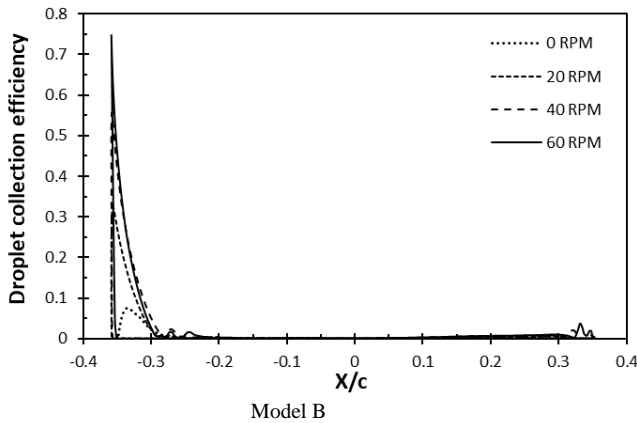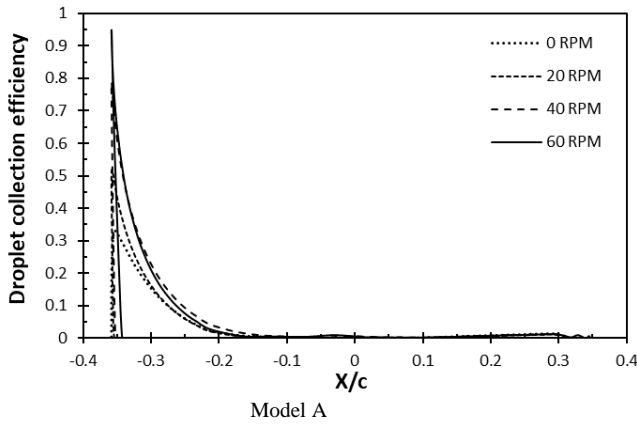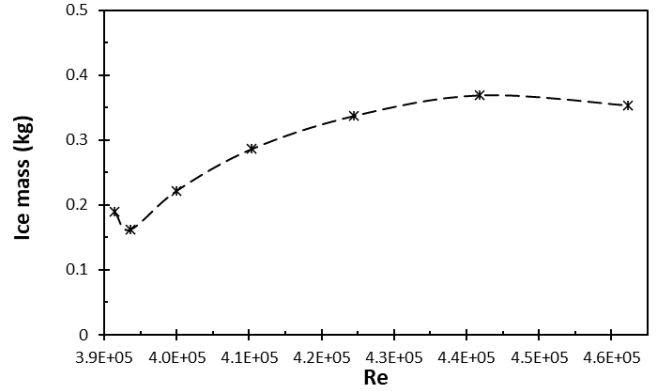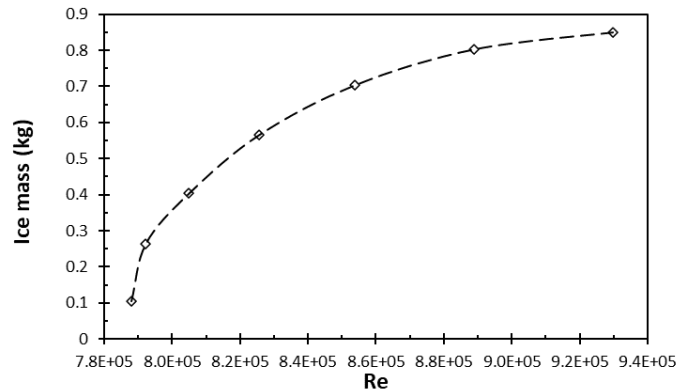

Model A

Model B
Figure 4. Droplet colletion efficiceny plots at variable RPM.

D. Ice mass accumulation

For case 1, the relative flow Reynolds number is calculated based on the characteristic chord length, rotational and linear speed over the blade section and flow properties. As illustrated in Fig. 5, higher Reynolds numbers (due to the increase in the characteristic length of the geometry, i.e. blade chord length and rotational speeds) significantly impact the quantity of ice accumulation.
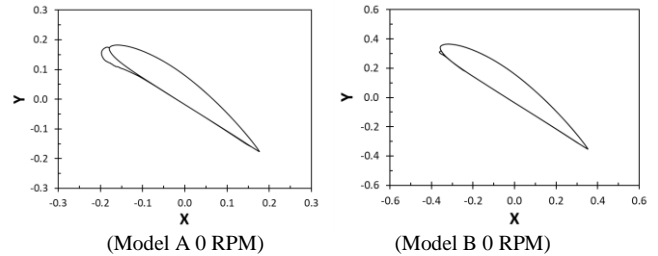

Model A

Model B
Figure 5. Ice quantities at variable relative flow Reynolds numbers.

E. Ice distribution

For case 1, ice shapes for both blade sections at varied rotational speeds are presented in Fig. 6. Ice shapes are formed at the leading edge of the blade where the majority of the droplet collection occurs. Results indicate that ice shapes on the smaller blade section, Model A, cover more surface area when compared to the larger blade. However, more ice mass accumulates on the larger blade, Model B. This suggests that ice horns are more likely to form on smaller blade sections, characterized by small chord lengths.
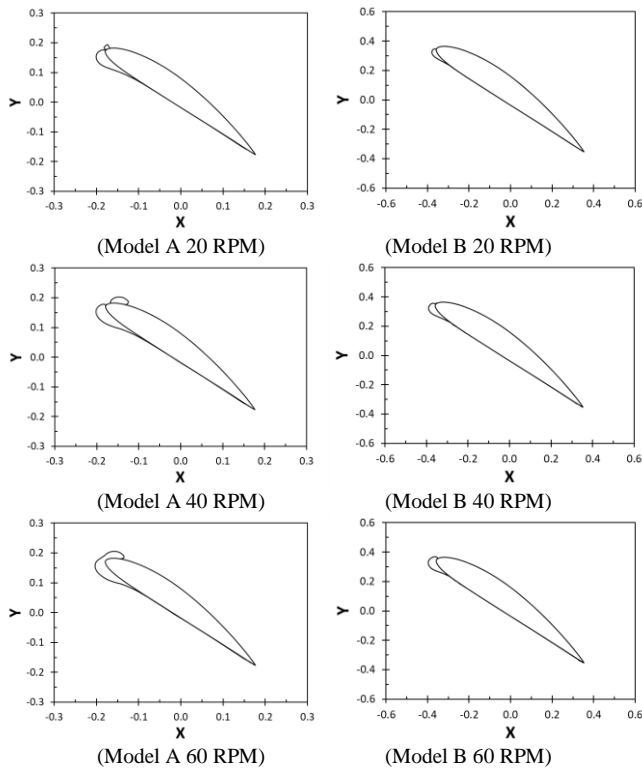

(Model A 0 RPM)

(Model B 0 RPM)

(Model A 20 RPM) (Model B 20 RPM)

(Model A 40 RPM) (Model B 40 RPM)

(Model A 60 RPM) (Model B 60 RPM)

Figure 6. Ice shapes around Model A (left) and Model B (right) at variable RPM.

F. Speed ratio and relative Reynolds number

For case 2, the relative flow Reynolds number and speed ratio over each blade section are maintained to investigate the significant changes in the (air and droplet) flow fields and ice accretion characteristics. The velocity field (Fig. 7) predicts an almost identical distribution of flow around both blade models, however, different velocity ranges for air and droplets are predicted. Predictions for the pressure coefficient show no significant changes over both blades on suction and pressure surfaces (Fig.8). Plots for droplet collection over both blade surfaces are presented in Fig. 9, which predict higher collection efficiency values for the smaller blade section, Model A. By comparison, the predicted ice shapes for both models are shown in Fig. 10. The predicted ice mass for the smaller blade section, Model A, is higher than the larger blade section, Model B, due to the higher velocity ranges over the smaller characteristic chord length of model A. This highlights the impact of maintaining both the relative flow relative number and speed ratio on the icing process.
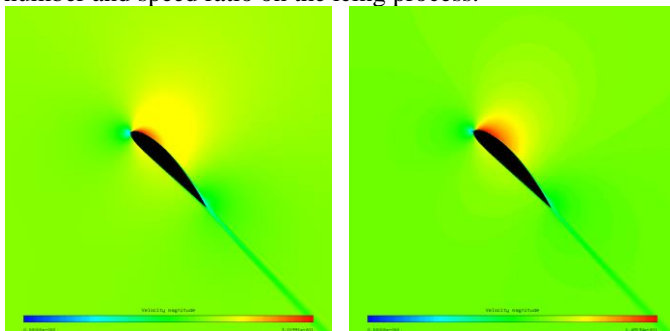
V_a (0 m/s - 30.1991 m/s) V_a (0 m/s - 14.9134 m/s)

V_d (0 m/s - 31.2418 m/s) V_d (0 m/s - 16.3441 m/s)

Figure 7. Flow field around Model A (left) and Model B (right) at same relative Reynolds number and speed ratio (air and droplet velocity ranges).
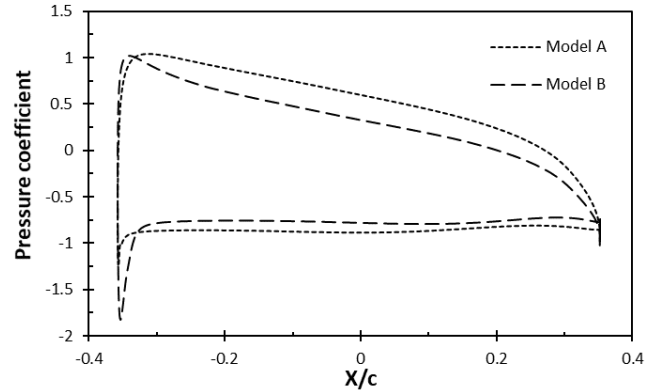

Figure 8. Pressure coefficients at same relative Reynolds number and speed ratio.
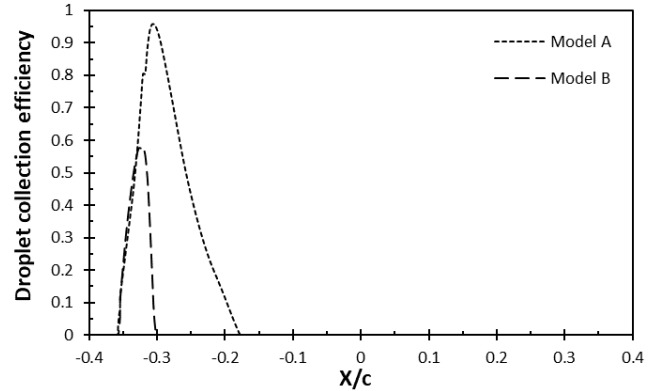

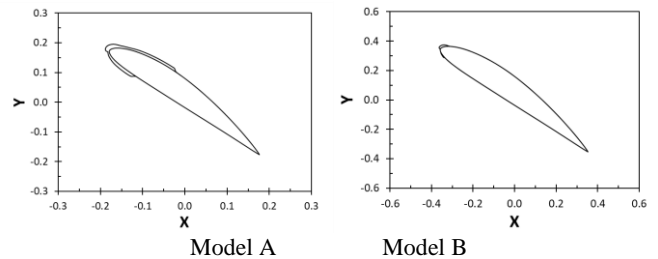Figure 9. Droplet colletion efficieny at same relative Reynolds number and speed ratio.

Model A   Model B

Figure 10. Formed ice shapes around both blade models at same relative Reynolds number and speed ratio.

G. Mass conservation and energy conservation

Considering cases 1 and 2, for both blade models, impinging water mass, ice mass and energy exchange due to water impingement, the convective heat transfer and ice formation are predicted and presented in Table 3. For case 1, predictions suggest the large blade section develops higher energy rates when compared to Model A. For case 1, predictions suggest the smaller blade section tends to have a slightly lower freezing fraction when compared to the larger blade. Higher energy rates during the freezing process occur at higher speeds.

For case 2, predictions suggest large differences in water collection magnitudes and ice masses between both models, when the relative Reynolds number and speed ratio are maintained on both models.

TABLE 3 TABULATED VALUES

CASE 1						
Model A						
Run No.	M_{imp} (kg)	M_{ice} (kg)	E_{imp} (kJ)	E_{ice} (kJ)	E_{conv} (kJ)	n
0 RPM	0.19	0.18	-4.82	65.44	57.34	0.94
10 RPM	0.21	0.16	-5.51	56.17	39.38	0.76
20 RPM	0.24	0.22	-6.25	76.72	58.90	0.91
30 RPM	0.30	0.28	-7.79	99.02	66.97	0.93
40 RPM	0.36	0.33	-9.35	116.67	74.96	0.91
50 RPM	0.41	0.36	-10.49	127.75	81.85	0.87
60 RPM	0.40	0.35	-10.19	122.30	76.63	0.87
CASE 2						
Model A						
Run No.	M_{imp} (kg)	M_{ice} (kg)	E_{imp} (kJ)	E_{ice} (kJ)	E_{conv} (kJ)	n
1	0.22	0.21	-4.69	74.37	42.01	0.95
CASE 1						
Model B						
Run No.	M_{imp} (kg)	M_{ice} (kg)	E_{imp} (kJ)	E_{ice} (kJ)	E_{conv} (kJ)	n
0 RPM	0.11	0.10	-2.77	36.01	23.62	0.90
10 RPM	0.26	0.26	-6.68	91.32	84.63	1
20 RPM	0.40	0.40	-10.21	139.57	129.35	1
30 RPM	0.56	0.56	-14.34	195.97	181.45	1
40 RPM	0.71	0.70	-17.84	243.71	224.97	0.98
50 RPM	0.81	0.80	-20.39	277.86	250.76	0.98
60 RPM	0.85	0.84	-21.62	294.19	260.65	0.98
CASE 2						
Model B						
Run No.	M_{imp} (kg)	M_{ice} (kg)	E_{imp} (kJ)	E_{ice} (kJ)	E_{conv} (kJ)	n
1	0.12	0.11	-3.12	40.6	25.4	0.91

IV. CONCLUSIONS

In this paper, scaling effects on the flow field and ice accretion on rotating wind blades are investigated at different flow conditions. Two similar NACA 4415 blade sections share a scale factor of 2. They are investigated numerically using ANSYS FENSAP ICE. Two cases are examined, one by rotating both similar sections at variable rotating speeds (i.e. ranges from 0 to 60 RPM) and same flow conditions, and the other case by maintaining the value of the relative flow Reynolds number and speed ratio over each similar blade section. For case 1, velocities over the two similar blades are almost similar in terms of the distribution of the flow around the blade at different RPM and slight changes are found in the magnitudes of the velocity ranges. More flow attachment on the suction side of the blade is found at higher RPM. The droplet collection is found at the leading edge for both blade models. A smaller blade section has more droplet collection efficiency magnitude when compared to the larger section, which demonstrates the resulting large icing area coverage over its surface. The relative flow Reynolds number greatly impacts ice mass. This suggests that large blade sections are characterized by large characteristic lengths compared to the

smaller sections (i.e. chord length), operating at the same flow conditions and rotational speeds, which can form more ice mass. Results showed that heat transfer rates and freezing fraction values during the icing process over the small blade section are slightly lower when compared to the large blade section. For case 2, results indicated higher velocity magnitudes over the small blade. Minimal changes are found in the pressure distributions between both blade sections. More droplet collection is found on the small blade section. Larger icing area coverage and ice mass are found over the small blade section. The results provide useful predictions for the changes in the flow field and ice accretion on wind turbine blade sections.

REFERENCES

[1] Feng, F., Li, S., Li, Y., & Tian, W. (2012). Numerical simulation on the aerodynamic effects of blade icing on small scale Straight-bladed VAWT. Physics Procedia, 24, 774-780.

[2] Battisti, L. (2015). Wind turbines in cold climates: Icing impacts and mitigation systems. Springer.

[3] Li, Y., Sun, C., Jiang, Y., & Feng, F. (2019). Scaling method of the rotating blade of a wind turbine for a rime ice wind tunnel test. Energies, 12(4), 627.

[4] Switchenko, D., Habashi, W., Reid, T., Ozcer, I., & Baruzzi, G. (2014). FENSAP-ICE Simulation of Complex Wind Turbine Icing Events, and Comparison to Observed Performance Data. In 32nd ASME Wind Energy Symposium (p. 1399).

[5] Sultana, K.R., Dehghani, S.R., Pope, K., & Muzychka, Y.S. (2017). Numerical techniques for solving solidification and melting phase change problems. Numerical Heat Transfer, Part B: Fundamentals: 129-145

[6] Ibrahim, G.M., Pope, K., and Muzychka, Y.S. (2018). Transient ice accretion on wind turbine blades. Wind Engineering 42(6): 596-606.

[7] Kraj, A. G., & Bibeau, E. L. (2010). Measurement method and results of ice adhesion force on the curved surface of a wind turbine blade. Renewable Energy, 35(4), 741-746.

[8] Reid, T., Baruzzi, G., Ozcer, I., Switchenko, D., & Habashi, W. FENSAP-ICE simulation of icing on wind turbine blades, part 1: performance degradation. In 51st AIAA aerospace sciences meeting including the new horizons forum and aerospace exposition (p. 750), Grapevine, Texas, (2013, January).

[9] Reid, T., Baruzzi, G., Ozcer, I., Switchenko, D., & Habashi, W. FENSAP-ICE simulation of icing on wind turbine blades, part 2: ice protection system design. In 51st AIAA Aerospace Sciences Meeting including the New Horizons Forum and Aerospace Exposition (p. 751), Grapevine, Texas, (2013).

[10] Ibrahim, G. M., Pope, K., & Muzychka, Y. S. (2018). Effects of blade design on ice accretion for horizontal axis wind turbines. Journal of Wind Engineering and Industrial Aerodynamics, 173, 39-52.

[11] Barber, S., Wang, Y., Jafari, S., Chokani, N., & Abhari, R. S. (2011). The impact of ice formation on wind turbine performance and aerodynamics. Journal of Solar Energy Engineering, 133(1).

[12] Homola, M. C., Wallenius, T., Makkonen, L., Nicklasson, P. J., & Sundsbø, P. A. (2010). Turbine size and temperature dependence of icing on wind turbine blades. Wind Engineering, 34(6), 615-627.

[13] Fu, P., & Farzaneh, M. (2010). A CFD approach for modeling the rime-ice accretion process on a horizontal-axis wind turbine. Journal of Wind Engineering and Industrial Aerodynamics, 98(4-5), 181-188.